



# Contrasting opacity of bridgmanite and ferropericlase in the lowermost mantle: Implications to radiative and electrical conductivity

Sergey S. Lobanov<sup>a,b,\*</sup>, François Soubiran<sup>c</sup>, Nicholas Holtgrewe<sup>b</sup>, James Badro<sup>d</sup>, Jung-Fu Lin<sup>e</sup>, Alexander F. Goncharov<sup>b</sup>

<sup>a</sup> GFZ German Research Center for Geosciences, Section 3.6, Telegrafenberg, 14473 Potsdam, Germany

<sup>b</sup> Earth and Planets Laboratory, Carnegie Institution of Washington, Washington, DC 20015, USA

<sup>c</sup> École Normale Supérieure de Lyon, Université Lyon 1, Laboratoire de Géologie de Lyon, CNRS UMR5276, 69364 Lyon Cedex 07, France

<sup>d</sup> Université de Paris, Institut de physique du globe de Paris, CNRS, 75005 Paris, France

<sup>e</sup> Department of Geological Sciences, Jackson School of Geosciences, The University of Texas at Austin, Austin, TX 78712, USA

## ARTICLE INFO

### Article history:

Received 26 November 2020

Received in revised form 24 February 2021

Accepted 3 March 2021

Available online xxxx

Editor: M. Ishii

### Keywords:

thermal conductivity

high pressure

time-resolved spectroscopy

core-mantle boundary

bridgmanite

ferropericlase

## ABSTRACT

Earth's lowermost mantle displays complex geological phenomena that likely result from its heterogeneous physical interaction with the core. Geophysical models of core-mantle interaction rely on the thermal and electrical conductivities of appropriate geomaterials which, however, have never been probed at representative pressure and temperature ( $P$ - $T$ ) conditions. Here we report on the opacity of single crystalline bridgmanite and ferropericlase and link it to their radiative and electrical conductivities. Our results show that light absorption in the visible spectral range is enhanced upon heating in both minerals but the rate of change in opacity with temperature is a factor of six higher in ferropericlase. As a result, bridgmanite in the lowermost mantle is moderately transparent while ferropericlase is highly opaque. Our measurements support previous indirect estimates of low ( $< 1$  W/m/K) and largely temperature-independent radiative conductivity in the lowermost mantle. This implies that the radiative mechanism has not contributed significantly to cooling the Earth's core throughout the geologic time. Opaque ferropericlase is electrically conducting and mediates strong core-mantle electromagnetic coupling, explaining the intradecadal oscillations in the length of day, low secular geomagnetic variations in Central Pacific, and the preferred paths of geomagnetic pole reversals.

© 2021 Elsevier B.V. All rights reserved.

## 1. Introduction

The observed vigor of plate tectonics, plume activity, and geodynamo requires that the present-day heat flow across the core-mantle boundary ( $Q_{CMB}$ ) is 8–16 TW (Lay et al., 2008; Nimmo, 2015). This estimate can be validated independently by employing the Fourier law of heat conduction:

$$Q_{CMB} = A_{CMB} * k_{total} * \Delta T, \quad (1)$$

where  $A_{CMB}$  is the surface area of the CMB,  $\Delta T$  is the temperature gradient in the thermal boundary layer (TBL), and  $k_{total}$  its thermal conductivity. Three microscopic mechanisms of heat transport contribute to  $k_{total}$ : lattice, electronic, and radiative thermal conductivities. While all of these contributions have never been mea-

sured at CMB  $P$ - $T$  conditions, radiative conductivity ( $k_{rad}$ ) is most uncertain with available estimates spanning 0.35–10 W/m/K (Goncharov et al., 2008, 2015; Hofmeister, 2014; Keppler et al., 2008; Lobanov et al., 2016, 2020). This enormous ambiguity in radiative conductivity, as well as the uncertainty in  $\Delta T$  and its global variation, precludes tighter constraints on the present-day  $Q_{CMB}$ . To better resolve the ability of the mantle to conduct heat via light radiation one needs to measure the optical absorption coefficients of representative lower mantle minerals at CMB  $P$ - $T$  conditions.

Independent of heat, solid mantle and liquid outer core may exchange angular momenta, which can produce observable variations in Earth's rotation. For example, electromagnetic coupling between the core and mantle may be responsible for the reversible change in the length of day with a period of  $\sim 6$  years (Holme and de Viron, 2013) as detected by geodetic techniques. Strong coupling, however, demands that the direct current (DC) electrical conductivity of the lower mantle minerals is sufficiently high at the CMB (Buffett, 1992). The absence of a significant lag between the rotational and magnetic signals impose a stringent limitation

\* Corresponding author.

E-mail address: slobanov@gfz-potsdam.de (S.S. Lobanov).

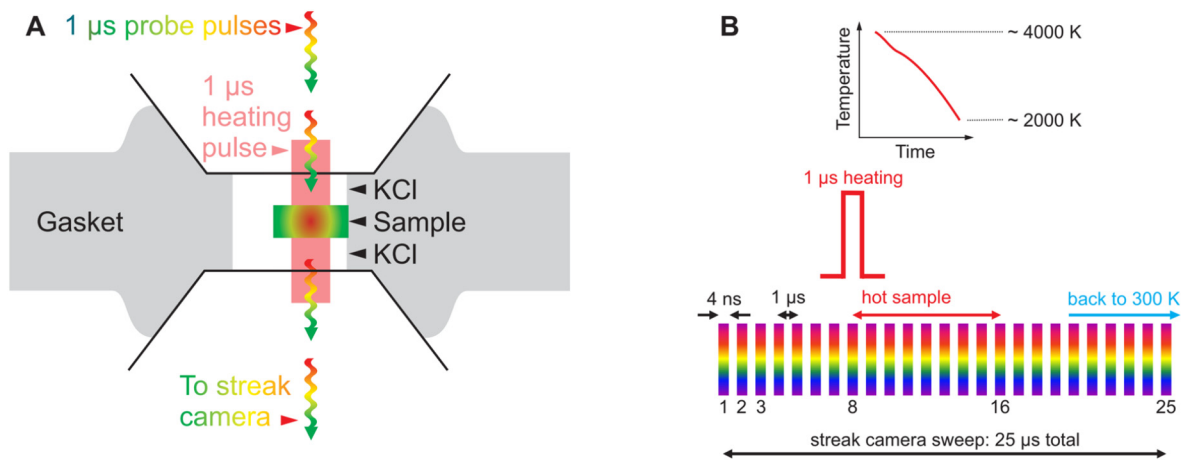


**Fig. 1.** (A) Diamond anvil cell assemblage used in this work. Samples were sandwiched between two KCl wafers and positioned in the cavity such that part of it can be used to measure optical reference (through KCl only). (B) Timing of the single-shot laser-heating experiments. Probe pulses (supercontinuum laser) traverse the sample every 1  $\mu$ s. The 1  $\mu$ s heating laser (1070 nm, double-sided) arrives at 8  $\mu$ s of the 25–30  $\mu$ s long streak camera sweep.

on the thickness of the conducting layer to be smaller than 50 kilometers (Holme and de Viron, 2013). Tomographic images of the lowermost mantle revealed anomalous 5–40 km thick patches directly above the core with strong seismic wave speed reductions of  $\sim 10\%$ , called ultra-low velocity zones (ULVZs) (Garnero and McNamara, 2008). Because of their location just above the CMB and small thickness, these patches may be responsible for the efficient core-mantle electromagnetic coupling, yet the electrical properties of ULVZs are unknown. The DC electrical conductivity can be constrained in optical absorption experiments by extrapolating the energy-dependent optical conductivity to zero frequency. Therefore, the radiative and DC electrical conductivities can be in principle determined in a single optical experiment.

The optical absorption coefficients of lower mantle minerals have never been measured at CMB  $P$ - $T$  conditions ( $P \sim 135$  GPa,  $T \sim 4000$  K). The brightness of conventional light sources is insufficient to probe hot samples with spectral radiance corresponding to several thousand degrees Kelvin and spectroscopic measurements at the conditions of combined high  $P$  and  $T$  remain a great challenge. As a consequence, information on the optical properties of mantle minerals at high  $P$  is largely limited to  $T < \sim 1000$  K. One notable exception is the recent report on the optical extinction coefficients (absorption + scattering) of a polycrystalline assemblage of mostly bridgmanite and ferropericlase (termed pyrolite) at  $P$  of up to 135 GPa and  $T$  of up to  $\sim 2800$  K that point to an ultra-low radiative conductivity at the CMB of  $\sim 0.35$  W/m/K (Lobanov et al., 2020). The use of a polycrystalline sample with submicron grains in this study allowed minimizing iron diffusion within the sample on the experimental time scale of a few seconds. However, disentangling the absorption and scattering contributions to the measured extinction coefficient of the polycrystalline sample was a principal challenge of that study (Lobanov et al., 2020).

Here, we overcome the experimental limitations associated with iron diffusion by reducing the laser-heating duration by a factor of up to  $\sim 10^6$ , thanks to the use of dynamically-heated diamond anvil cells (DACs) coupled with laser-bright broadband pulsed optical probes and a fast detector. We report the optical absorption coefficients of single crystalline bridgmanite (Bgm), ferropericlase (Fp), and their polycrystalline  $\sim 4:1$  aggregate (synthesized from homogeneous pyrolite glass as is described by Lobanov et al. (2020)) to show that temperature is a major factor that governs the opacity near the base of the mantle where Bgm remains moderately transparent in the visible range while Fp is highly opaque. We reinforce our experimental findings with first-principles calculations of Fp optical properties at near CMB con-

ditions, which constrain its absorption coefficient in the near-IR range as well as the electrical conductivity. Our results indicate low radiative contribution to the  $Q_{CMB}$  and have profound implications to energy transport and electromagnetic coupling across the core-mantle boundary.

## 2. Methods

### 2.1. Diamond anvil cell and sample assembly

Rhenium gaskets were indented by compression to a pressure of  $\sim 30$  GPa in DACs equipped with beveled anvils having 100/300 and 80/300  $\mu$ m culets. Subsequently, circular holes with a diameter of  $\sim 50$   $\mu$ m were laser-drilled in the center of the indentation to serve as sample containers. After the drilling, the gaskets were washed in isopropanol for 30 min and mounted between the diamond anvils. Prior to positioning the sample, wafers of dry KCl (5  $\mu$ m thick) were centered on each of the anvil. Next, double-polished single crystals of ferropericlase ( $\text{Mg}_{0.87}\text{Fe}_{0.13}\text{O}$ , referred to as Fp13), bridgmanite ( $\text{Mg}_{0.94}\text{Fe}_{0.04}^{2+}\text{Fe}_{0.02}^{3+}\text{Al}_{0.01}\text{Si}_{0.99}\text{O}_3$ , referred to as Bgm6), and pyrolite glass with initial thickness of  $\sim 8$ –16  $\mu$ m were put into the sample cavity such that a sufficient area of the sample cavity was not covered by the sample to allow for reference transmission measurements through KCl (Fig. 1A). Synthesis procedures for these samples have been reported elsewhere (Lobanov et al., 2020; Lobanov and Speziale, 2019; Mao et al., 2017). Finally, the cells were brought to a desired pressure as gauged either by the position of the diamond Raman edge (Akahama and Kawamura, 2006) or ruby fluorescence (Syassen, 2008). We assume that the typical discrepancy between these two scales of  $< 5\%$  is the ambiguity in pressure. No correction for thermal pressure was applied since added thermal pressure is smaller than 5 GPa at 3000 K (Goncharov et al., 2007; McWilliams et al., 2016).

### 2.2. Static optical measurements at high pressure and 300 K

Here we used a custom-built all-reflective microscope combined with an IR, VIS, and near-UV conventional (non-laser) light sources. For the visible and near-UV range we used a fiber-coupled halogen-D<sub>2</sub> lamp focused to a  $\sim 50$   $\mu$ m spot on the sample. The transmitted portion of the radiation was collimated by a 20  $\mu$ m pinhole and sent to the spectrograph (Acton Research Corporation SpectraPro 500-i) equipped with a 300 grooves/mm grating and a CCD chilled to 235 K. Measurements in the IR range were performed on the same optical bench but with a Fourier transform

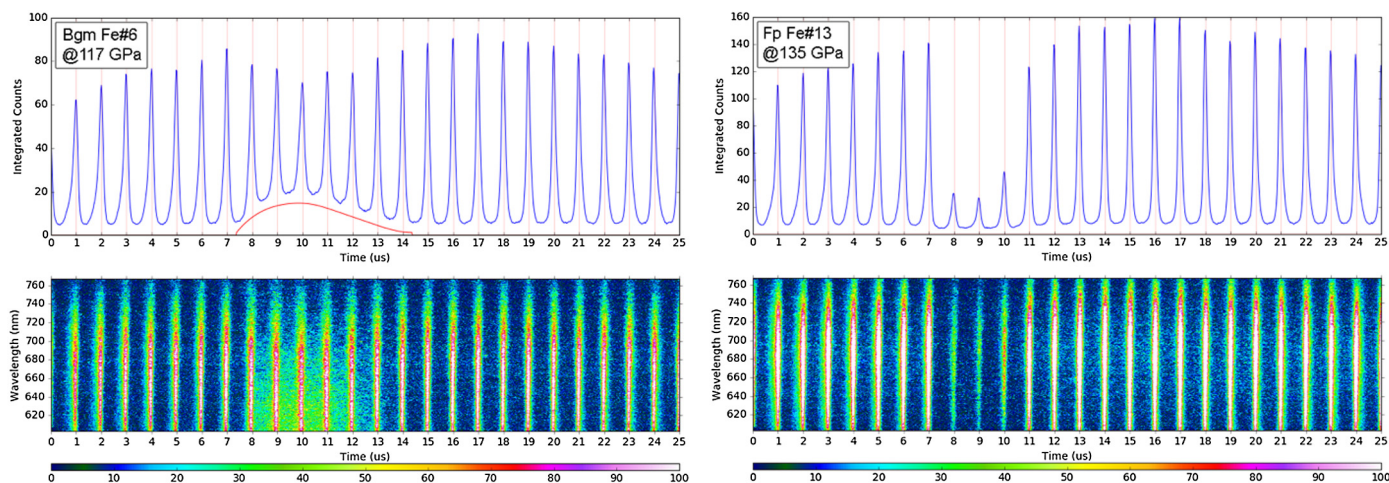


**Fig. 2.** Representative streak camera images (bottom panels) and corresponding integrated intensity (top panels) of Bgm6 at 117 GPa (left) and Fp13 at 135 GPa (right). The 1  $\mu$ s laser heating pulse arrived at  $\sim 8^{\text{th}}$  microsecond heating the samples to a maximum temperature of  $\sim 4000$  K (Bgm) and  $\sim 3000$  K (Fp), in these particular shots. Note the presence of apparent thermal background in the case of bridgmanite (top panel, red curve). (For interpretation of the colors in the figure(s), the reader is referred to the web version of this article.)

spectrometer equipped with a quartz beamsplitter (Varian Resolution Pro 670-IR). Details of our IR-VIS-UV setup have been reported in our previous publications (Goncharov et al., 2009, 2015; Lobanov et al., 2015, 2017b). Overall, this setup allows for a high-quality absorption spectrum in a wide spectral range (2500–30000  $\text{cm}^{-1}$ ) at room temperature. Absorption coefficient was evaluated as  $\alpha(\nu) = \ln(10) * \frac{1}{d} * (-\log_{10}(I_{\text{sample}} - I_{\text{bckg}}) / (I_{\text{reference}} - I_{\text{bckg}}))$ , where  $d$  is sample thickness at high pressure (measured by 3D profilometry on decompressed samples as detailed in the Supplementary Information),  $I_{\text{sample}}$  is the intensity of light transmitted through the sample,  $I_{\text{reference}}$  is the intensity of light passed through the KCl pressure medium, and  $I_{\text{bckg}}$  is the background reading. Light losses due to the reflections at the sample-KCl interfaces are small ( $< 1\%$ ) due to the similarity of the KCl and samples' refractive index at  $P > 100$  GPa ( $n \sim 2$ ) and were not taken into account.

### 2.3. Static optical measurements at high pressure and $T < \sim 2000$ K

Overall, static optical measurements at continuous laser heating allow probing the sample by a large number of probe pulses, which improves the quality of the resulting absorption spectra as compared to spectroscopic measurements in dynamic experiments. The experimental setup combines a quasi-continuous Yt-doped 1070 nm fiber laser, a pulsed Leukos Pegasus ultra-bright supercontinuum (broadband,  $\sim 4000$ – $25000$   $\text{cm}^{-1}$ ) probe operating at 1 MHz, and an intensified gated CCD detector (Andor iStar SR-303i-A). The confocal probe spot size ( $\sim 5$   $\mu\text{m}$ ) was smaller than the heating laser spot ( $\sim 15$   $\mu\text{m}$ ). The spectral collection was initiated 500 ms after the start of a 1 s laser heating cycle. The detector gates were modulated for 200 ms at a rate of  $\sim 41$  kHz and synchronized with the probe pulses (4 ns pulse width). Probe brightness was maximized to achieve maximum signal through the reference KCl without saturating the detector. The precise synchronization of the probe pulses and detector gates diminishes thermal background, drastically improves the signal-to-background ratio, and allows optical absorbance measurements in the VIS range ( $\sim 13000$ – $22500$   $\text{cm}^{-1}$ ) up to  $\sim 2000$  K. High-temperature absorption coefficients were evaluated as  $\alpha(\nu) = \ln(10) * \frac{1}{d} * (-\log_{10}(I_{\text{sample}}^T - I_{\text{bckg}}^T) / (I_{\text{reference}} - I_{\text{bckg}}))$ , where  $I_{\text{sample}}^T$  and  $I_{\text{bckg}}^T$  are the probe and background intensity at high temperature. Temperature was measured from both sides of the sample by imaging the hot spot onto the intensified CCD detector array. In static measurements, the error in temperature is standard to that typically

assumed for the laser-heated DAC method ( $\pm 200$  K). Further details of this setup are provided in Lobanov et al. (2016).

### 2.4. Dynamic optical measurements at high pressure and $T > \sim 2000$ K

To succeed in measuring optical absorption at CMB conditions we performed dynamically-heated experiments with transient optical probing, which is the main novelty of the present work (Fig. 1A). This experimental setup combines the same heating and probe lasers (see above) but spectral measurements were performed by a Sydor ROSS 1000 streak camera on a Princeton Instruments spectrometer ( $f/4$ , 150 grooves/mm). Together these components enable single-pulse laser heating coupled with *in situ* time-resolved absorption measurements at  $T > \sim 2000$  K (Jiang et al., 2018). Typical streak camera sweeps were 25–30  $\mu\text{s}$  long and, accordingly, recorded 25–30 pulses of the 1 MHz probe each of which can be used for spectra evaluation (Fig. 1B). Importantly, spectral features and intensity of individual supercontinuum pulses are sufficiently reproducible to allow for single pulse spectroscopy (as is shown in this work). After initiation of the streak camera image collection, a single 1  $\mu\text{s}$  long pulse of the 1070 nm fiber laser arrives at the  $8^{\text{th}}$   $\mu\text{s}$  to heat the sample (Fig. 1B), allowing for a sufficient number of probe pulses to traverse the sample prior to heating. Sample absorption at high temperature was recorded by the streak camera images (Fig. 2) taken at two distinct grating positions centered at 700 and 590 nm, accessing 15000–20000 and 13000–16400  $\text{cm}^{-1}$  spectral ranges, respectively. From streak camera images the absorption coefficient was evaluated as:  $\alpha(\nu) = \ln(10) * \frac{1}{d} * (-\log_{10}(I_{\text{sample}}^{\text{time}} - I_{\text{bckg}}^{\text{time}}) / (I_{\text{reference}} - I_{\text{bckg}}))$ , where  $I_{\text{sample}}^{\text{time}}$  and  $I_{\text{bckg}}^{\text{time}}$  are the probe intensity at a given time and the corresponding (thermal) background. Similarly to the static optical experiments, reflection losses were unimportant.

Overlapping absorption spectra were stitched together to produce a spectrum in the 13000–20000  $\text{cm}^{-1}$  range (Fig. 3). Immediately after the collection of streak camera images the probe laser was blocked and streak camera images were measured again at identical laser heating power in order to obtain  $I_{\text{bckg}}^{\text{time}}$ . Temperature measurements at the 700 and 590 nm grating positions generally yielded consistent results. However, temperature measurements with the grating centered at 590 nm often yielded temperatures lower than that at obtained at the 700 nm grating position (up to 1200 K lower). To assign temperatures to stitched spectra we relied on radiometry measurements with the grating centered at 700 nm,

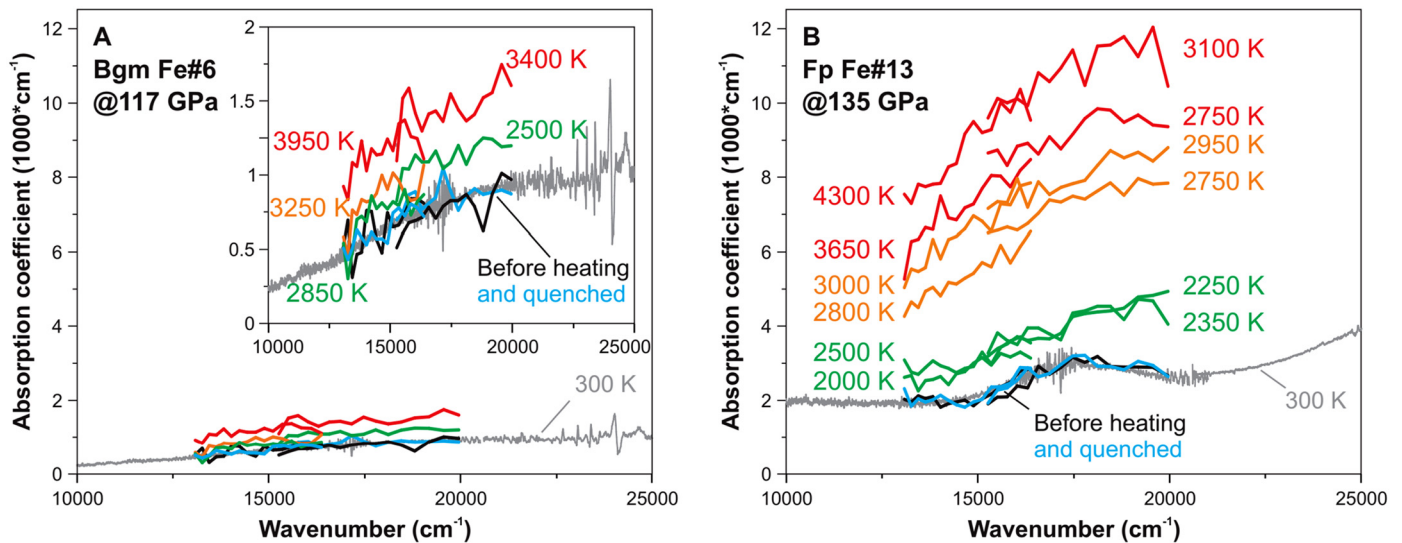


**Fig. 3.** Absorption coefficients of bridgmanite at 117 GPa (A) and ferropericlasite at 135 GPa (B). Black – prior to the heating pulse arrival (1–7  $\mu$ s); red, orange, or green – upon cooling at high temperature (9–16  $\mu$ s); and blue – after cooling (20–25  $\mu$ s). The spectra are labeled by apparent temperatures measured immediately after the absorbance measurements at identical laser heating power. The discrepancy in temperature among the overlapping spectra is probably due to less reliable temperature measurements in experiments at higher frequencies (15000–20000  $\text{cm}^{-1}$ ). The assignment of temperature to the measured spectra was based on the lower frequency spectral range (13100–16400  $\text{cm}^{-1}$ ), which also yields more conservative estimate of opacity. Inset in (A) is a close-up view of Bgm6 data. Temperature uncertainty is  $< \pm 500$  K. Grey spectra are absorption coefficients measured prior to heating with a conventional absorption spectroscopy setup (Goncharov et al., 2009). Corresponding wide-range spectra (near-IR to UV) at 300 K are shown in Fig. S1.

as more light was available for Planck fitting, which improves the reliability in temperature determination. We could only observe sufficiently intense thermal background ( $> 10$  counts in a single streak camera sweep) at  $T > \sim 3000$  K. To characterize sample absorbencies at lower temperatures, up to 100 consecutive streak camera sweeps were accumulated at low laser heating power to improve the statistics, assuming that the coupling of the sample to the heating laser did not change substantially over the 100 heating cycles. In all cases, the sample absorbance was checked afterwards to ensure its reversibility over the heating cycles.

We empirically estimate the overall temperature uncertainty based on the reproducibility of the absorption coefficients at high temperatures. At  $T > 2000$  K, the reproducibility of the absorption coefficients was typically within 0–20%, which translates to the overall ambiguity in the temperature measurements of  $\pm 500$  K. This estimate is independently confirmed by optical observations of dark spots (presumably Fe-rich and formed upon melting) and increased room-temperature absorbencies in samples quenched from temperatures exceeding their expected solidus.

### 3. Results and discussion

First, we collected high-pressure wide spectral range absorption coefficients of double-polished single crystalline Bgm6 (Bgm with 6 mol.% Fe) and Fp13 (Fp with 13 mol.% Fe) (Fig. S1) using a conventional optical absorption setup that allows high-quality measurements at room temperature (Goncharov et al., 2009). These absorption spectra reveal the distinct light absorption mechanisms that may contribute to the opacity of Bgm and Fp in the lowermost mantle. Intervalence  $\text{Fe}^{2+}$ - $\text{Fe}^{3+}$  charge transfer (CT) gives rise to the broad absorption band at  $\sim 17000$   $\text{cm}^{-1}$  in the spectrum of Bgm6 ( $\text{Mg}_{0.94}\text{Fe}_{0.04}^{2+}\text{Fe}_{0.02}^{3+}\text{Al}_{0.01}\text{Si}_{0.99}\text{O}_3$ ), which is close in composition to that expected for Bgm in the lower mantle (Mao et al., 2017). Crystal field ( $d$ - $d$ ) bands were not observed in the thin ( $\sim 6$   $\mu\text{m}$  at 117 GPa) and relatively iron-poor sample studied here, as was also the case in the previous high-pressure studies of lower mantle Bgm (Goncharov et al., 2015; Keppler et al., 2008). The spectrum of Fp13 showed three multiplicity-allowed low spin

$\text{Fe}^{2+}$  bands. Both Bgm6 and Fp13 have a distinct UV absorption edge, typically assigned to the Fe-O CT (Burns, 1993).

We continued with dynamic experiments in which the samples were heated by a single 1  $\mu$ s long near-infrared (1070 nm) laser pulse and probed by an ultra-bright broadband pulsed laser. Thermal radiation emitted off the dynamically-heated samples vanishes in streak camera images within  $\sim 10$   $\mu$ s following the arrival of the heating pulse (Fig. 2). Finite-element modeling of time-dependent thermal fluxes in a pulsed laser-heated DAC also indicates that  $\sim 10$   $\mu$ s is sufficient to restore sample's temperature back to 300 K, thanks to the high thermal conductivity of diamond (Montoya and Goncharov, 2012). Accordingly, the probe pulse train arriving with an interval of 1  $\mu$ s traverses distinct thermal states and records the spectroscopic information in time domain. The timing of our dynamic experiments also allows extracting room-temperature absorption spectra prior to the arrival of the heating laser and after quenching. The obtained room-temperature spectra were in good agreement with our wide-range spectra.

Upon heating of Bgm6 to  $\sim 2500$  K its absorption coefficient ( $\alpha$ ) is enhanced by approximately a factor of two (Fig. 3), translating into a relatively small rate of increase in opacity averaged over the visible range:  $\Delta\alpha/\Delta T$  of  $\sim 0.05$   $\text{cm}^{-1}/\text{K}$  (Fig. 4). At  $T > \sim 3000$  K, Bgm6 visible range opacity increases much more rapidly with  $\Delta\alpha/\Delta T = 0.4$   $\text{cm}^{-1}/\text{K}$ , suggesting a crossover to a more efficient light absorption mechanism in Bgm across the temperature range of the TBL. Similarly, the opacity of Fp13 is enhanced at  $T > 2000$  K but with a rate that is approximately six times faster than in Bgm6 ( $\Delta\alpha/\Delta T = 2.5$   $\text{cm}^{-1}/\text{K}$ ). Specific absorption bands are no longer resolved in the high-temperature spectra of Bgm6 and Fp13 and the visible range opacity is evidently governed by a reversible temperature-induced red-shift of the Fe-O CT (UV absorption edge). Indeed, the initial room-temperature absorption coefficients of Bgm6 and Fp13 are restored after the samples cool down to 300 K. The reversibility in opacity over the heating cycles indicates that our pulsed laser heating time domain experiments probe intrinsic temperature-induced changes in the electronic structure as opposed to extrinsic iron redistribution due to temperature gradients in continuously laser-heated sample.

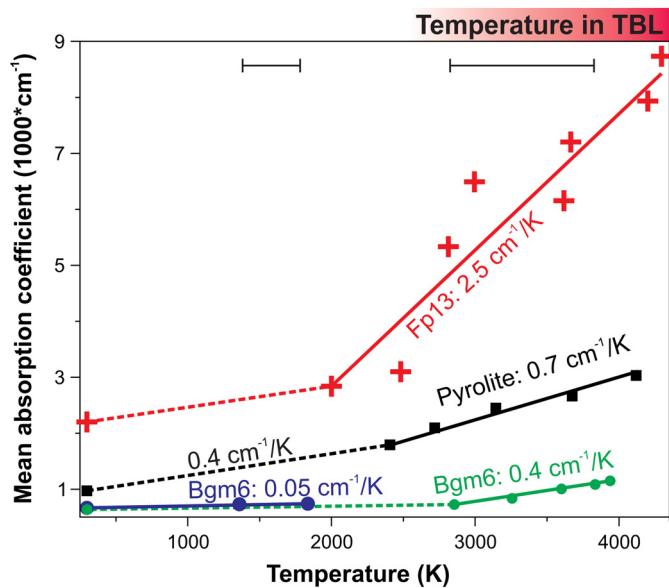


**Fig. 4.** Temperature dependence of the mean absorption coefficients (13100–16400  $\text{cm}^{-1}$ ) observed in dynamic laser-heating experiments on bridgmanite at 117 GPa (Bgm6, green), ferropericlasite at 135 GPa (Fp13, red), and pyrolite at 130 GPa (black). Dashed lines show an extrapolation from the 2500–3000 K data to 300 K. The violet solid line shows the mean absorption coefficient of Bgm6 obtained in static laser-heating experiments (Fig. S2), which is in agreement with that reported previously ( $\sim 0.08 \text{ cm}^{-1}/\text{K}$  at  $\sim 1600$ – $2500 \text{ K}$ ) for the same crystal at 87 GPa (Lobanov et al., 2020). Error bars indicate the temperature uncertainty of  $\sim \pm 500 \text{ K}$  and  $\sim \pm 200 \text{ K}$  in dynamic ( $T > 2000 \text{ K}$ ) and static ( $T < 2000 \text{ K}$ ) experiments, respectively. The red bar above the figure depicts the temperature increase expected in the thermal boundary layer (TBL).

To gain quantitative information on the opacity of Bgm and Fp at  $T < 2000 \text{ K}$  the same DAC loadings were used for static optical absorption experiments in which the samples were continuously laser-heated for 1 s and probed by the broadband pulsed laser synchronized with a gated detector. Heating of Bgm6 to  $\sim 2000 \text{ K}$  results in a slight decrease of its  $\text{Fe}^{2+}$ - $\text{Fe}^{3+}$  CT band intensity while the contribution of the UV absorption edge is enhanced (Fig. S2). This static experiment reveals the competition of individual light absorption mechanisms in Bgm6 at  $T < 2000 \text{ K}$ , which is the cause of the relatively small net increase of its opacity in this temperature range ( $\Delta\alpha/\Delta T = 0.05 \text{ cm}^{-1}/\text{K}$ ), in excellent agreement with the rate inferred from the dynamic experiments described above (Fig. 4). Unfortunately, in static experiments on Fp13 we could not achieve satisfactory spectra reversibility at  $T > 1000 \text{ K}$ , which we tentatively assign to Soret-like iron diffusion due to the unavoidable temperature gradients in a laser-heated DAC. Note that the iron diffusivity in Fp is several orders of magnitude higher than in Bgm (Ammann et al., 2011). The use of a single and short laser-heating pulse in dynamic experiments described in this work allowed us to suppress this unwanted irreversible effects in single crystals and build up on our previous study of pyrolite optical properties at static  $P$ - $T$  conditions (Lobanov et al., 2020).

The crossover in the slope of  $\Delta\alpha/\Delta T$  in Bgm and Fp at  $T > 2000 \text{ K}$  indicates a transition to the opacity regime dominated by the Fe-O CT, which is centered in the UV and is much more intense than  $d$ - $d$  or  $\text{Fe}^{2+}$ - $\text{Fe}^{3+}$  transitions because electronic states of different parity ( $d$  and  $p$ ) are involved in the excitation. Thus, the visible range opacity of Bgm and Fp in the lowermost mantle is governed by the Fe-O  $p$ - $d$  orbital overlap. Iron in the studied Bgm6 sample is predominantly eightfold-coordinated (distorted pseudododecahedral site) (Mao et al., 2017) while Fp hosts iron exclusively at the octahedral site. The  $p$ - $d$  orbital overlap at the sixfold site in Fp is definitely larger than that at the eightfold site in Bgm by virtue of a shorter Fe-O bond in Fp. As a result, the contri-

bution of the Fe-O CT to the visible range absorbance is stronger in Fp and the corresponding  $\Delta\alpha/\Delta T$  (i.e. temperature-induced red-shift) is a factor of six higher than in Bgm. Temperature-induced red-shifts of the Fe-O CT band have been identified in many ferromagnesian minerals at relatively low pressure and  $T < 1700 \text{ K}$  (e.g. Refs. (Burns, 1993; Lobanov et al., 2016; Shankland et al., 1979)), but the effect this mechanism bears on the lower mantle opacity and by extension its transport properties has never been quantified.

To understand the combined effect of Bgm and Fp on the opacity of the lower mantle in a realistic representative composition, we performed dynamic-heating optical experiments on pyrolite at 130 GPa and up to  $\sim 4000 \text{ K}$  (Fig. S3). We find that at  $T > 2500 \text{ K}$  the absorption coefficient of pyrolite increases with  $0.7 \text{ cm}^{-1}/\text{K}$ , in excellent agreement with the expectation ( $\Delta\alpha/\Delta T = 0.8 \text{ cm}^{-1}/\text{K}$ ) for a hypothetical 4:1 mechanical mixture of Bgm with Fp (i.e. constructed by weighing the opacity slopes of Bgm and Fp (Fig. 4) with their approximate volume fractions in the pyrolite model). Extrapolating dynamic-heating data to  $T < 2500 \text{ K}$  points to a factor of two smaller  $\Delta\alpha/\Delta T$  of  $\sim 0.4 \text{ cm}^{-1}/\text{K}$ , also in agreement with that reported recently for the same pyrolite sample but in static-heating optical experiments at 135 GPa and  $T < 2700 \text{ K}$  (Lobanov et al., 2020). The derived absolute value of the mean absorption coefficient at 300 K for such a pyrolite composition is sensitive to the scattering correction applied to compensate for light scattering on grain boundaries. Here, we estimated the contribution of scattering to the measured light extinction coefficient (absorption coefficient + scattering coefficient) in pyrolite based on the 300 K absorption coefficients of Bgm6 and Fp13 (Fig. S1), which is appropriate because scattering is negligible in single crystals. First, we constructed a hypothetical room-temperature absorption coefficient of the mechanical mixture of Bgm6 with Fp13 in the 4:1 proportion (pyrolite model) to infer that at 300 K the mean absorption coefficient of pyrolite in the visible range is  $\sim 1000 \text{ cm}^{-1}$ . The scattering coefficient at 300 K is then obtained by subtracting the value of  $1000 \text{ cm}^{-1}$  from the pyrolite extinction coefficient measured at 300 K. Assuming light scattering does not change significantly with  $T$ , we obtain the absorption coefficients of pyrolite at high  $T$  from the measured extinction coefficients by subtracting the scattering contribution (Fig. S3). In any case, the extracted values of  $\Delta\alpha/\Delta T$  for pyrolite (Fig. 4) are robust as they do not depend on the scattering correction. This assumption of a temperature-independent scattering coefficient is rather accurate as values of  $\Delta\alpha/\Delta T$  expected for the hypothetical 4:1 mechanical mixture of Bgm and Fp (pyrolite model) based on the single crystal measurements and that measured directly in pyrolite are in excellent agreement. Significant grain growth over the 1  $\mu\text{s}$  heating cycle, which would affect the scattering at high  $T$ , can also be ruled out since the temperature-enhanced absorbance of pyrolite is fully reversible (Fig. S3).

In addition to the visible range opacity, we need to constrain the opacity in the near-IR spectra range, where most of the radiative flux is expected at all plausible mantle temperatures. Towards this end, we computed the electronic structure of  $(\text{Mg}_{0.875}\text{Fe}_{0.125})\text{O}$  (Supplementary Information) at  $P$ - $T$  conditions mimicking that in our optical experiments (135 GPa, 4300 K). The computed electronic density of states (DOS) shows a non-zero density of  $d$ -electrons at the Fermi level due to the overlapping iron  $d$ -orbitals (Fig. S4). Local projection of the states identifies the peak centered at  $-1 \text{ eV}$  as the  $t_{2g}$  states and the peak centered at  $+1 \text{ eV}$  as the  $e_g$  states of iron, both mixed with oxygen  $p$  states. Electronic excitations between the occupied (centered at  $-1$  and  $+0.5 \text{ eV}$ ) and unoccupied (centered at  $+1 \text{ eV}$ ) states give rise to the distinct absorption bands observed at  $\sim 0.5$  and  $\sim 2 \text{ eV}$  (Fig. S5). Oxygen  $p$ -electrons also have non-zero DOS near the  $-1$  and  $+1 \text{ eV}$  levels and likely contribute to the observed absorption because

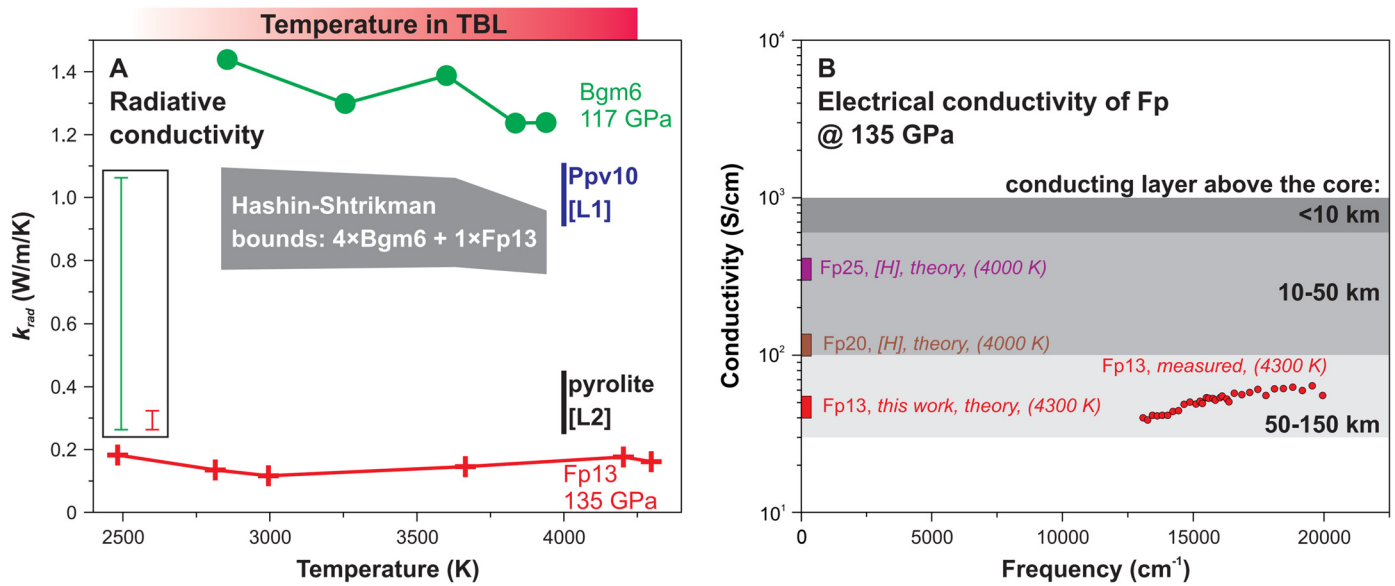


**Fig. 5.** (A) Radiative conductivity of ferroperricite ( $Mg_{0.87}Fe_{0.13}O$ ) and bridgmanite ( $Mg_{0.94}Fe_{0.04}Fe_{0.02}^{2+}Fe_{0.01}^{3+}Al_{0.01}Si_{0.99}O_3$ ) at the  $P$ - $T$  conditions of the lowermost mantle. The corresponding Hashin-Shtrikman bounds (Hashin and Shtrikman, 1962) for a mixture of 80 vol.% Bgm and 20 vol.% Fp are shown in grey. The vertical black and dark blue bars are previous estimates of radiative conductivity for pyrolite (Lobanov et al., 2020) and post-perovskite (Lobanov et al., 2017a), respectively. The green and red vertical bars in the inset are error bars estimated as 30% of the  $k_{rad}$  value (Supplementary Information). The horizontal red bar above the figure depicts the temperature increase expected in the thermal boundary layer (TBL). (B) Optical conductivity of ( $Mg_{0.87}Fe_{0.13}O$ ) measured at 135 GPa and 4300 K (red circles) and the corresponding DC electrical conductivity (red rectangle). Values for DC electrical conductivity of Fp with higher iron content are from Holmstrom et al. (2018). The grey shaded areas depict the ranges of Fp DC conductivity that would provide a conductance of  $10^8$  S in the lowermost 10, 10-50, and 50-150 km when arithmetically averaged with insulating Bgm (0.03 S/cm) (Sinmyo et al., 2014) in the 1:4 proportion (pyrolite model). The conductance of  $10^8$  S is required for the core-mantle electromagnetic coupling sufficient to produce the observed 6 year component in the length of day fluctuations (Buffett, 1992; Holme and de Viron, 2013).

of its higher probability for odd-parity states. We conclude, therefore, that both crystal field ( $d-d$ ) and Fe-O CT ( $p-d$ ) transitions are important mechanisms of Fp opacity at CMB conditions.

We model radiative thermal conductivity ( $k_{rad}$ ) in the TBL above the CMB using the experimentally-measured absorption coefficients of Fp and Bgm at 117-135 GPa and 2500-4300 K. The measured absorption coefficients of Fp were extrapolated to 3000  $cm^{-1}$  and 25000  $cm^{-1}$  using the Smith-Drude model that allows for a smooth decrease in the absorption coefficient with frequency (Fig. S6A). Using this lower bound constraint on the Fp13 absorption coefficient we can now obtain its radiative thermal conductivity (Supplementary Information):  $\sim 0.2$  W/m/K at 135 GP and 2500-4300 K (Fig. 5A). By extrapolating the absorption coefficients of Bgm6 in a similar fashion (Fig. S6B) we obtain a radiative conductivity in the range of  $\sim 1.2$ - $1.4$  W/m/K at  $T \sim 3000$ - $4000$  K (Fig. 5A). The radiative conductivity of Bgm may be sensitive to the not-yet-constrained  $Fe^{3+}$  content of this phase in the lower mantle. Our anticipation is that ferric iron at the pseudododecahedral site A of Bgm would only have a minor effect on the opacity of Bgm at  $T > 2000$  K because, as discussed above, the opacity is governed by the  $p-d$  overlap of octahedrally-coordinated iron. By the same logic, the substitution of Si for  $Fe^{3+}$  at the octahedral site B (Hummer and Fei, 2012) would increase the opacity of Bgm at high temperature. In any case, the obtained  $k_{rad}$  values of Bgm and Fp are upper bounds because both these phases are expected to show absorption bands in the IR, which we did not take into account in evaluating radiative conductivity. This may be the reason for the apparent disagreement with the pyrolite  $k_{rad}$  model which in turn relies heavily on the scattering correction (Lobanov et al., 2020). The geophysical significance of our estimates of radiative conductivity is secondary because it is approximately four times smaller than the most conservative estimates of lattice thermal conductivity of  $\sim 4$ - $5$  W/m/K (Tang et al., 2014). Most previous estimates of lattice thermal conductivity at the base of the mantle, however, group at  $\sim 6$ - $14$  W/m/K (Geballe et al., 2020; Haigis et al.,

2012; Hsieh et al., 2017, 2018; Manthilake et al., 2011; Ohta et al., 2017, 2012; Okuda et al., 2020, 2017; Stackhouse et al., 2015).

The radiative conductivity of Bgm and Fp at high  $P$ - $T$  conditions is essentially temperature-invariant, unlike that of semi-transparent materials where  $k_{rad} \sim \frac{T^3}{\alpha(P,T)}$  (Clark, 1957). Evidently, the transfer of radiative energy in the lowermost mantle is diminished by the temperature-induced opacity of Fp and Bgm revealed here. Assuming appropriate volume fractions of Bgm and Fp in the pyrolitic model (0.8 and 0.2) we obtained the Hashin-Shtrikman bounds (Hashin and Shtrikman, 1962) on the effective radiative conductivity in the lowermost mantle (Fig. 5A). The present results indicate that the radiative conductivity remains largely constant across the TBL and is smaller than  $\sim 1$  W/m/K. The absorption coefficient of post-perovskite is about two times higher than that of Bgm at the total iron content of  $\sim 10$  mol.% but shows a qualitatively similar temperature-dependence of its individual absorption bands (Lobanov et al., 2017a) to that observed in Bgm in this work due to their crystal chemical similarity. Therefore, the inclusion of post-perovskite into the model would result in lower radiative conductivity values.

Our DFT computations also indicate that the electronic contribution to the total thermal conductivity is non-negligible and is  $\sim 1$  W/m/K (Fig. S7), which is consistent with the estimate of Holmstrom et al. (2018) for Fp with 19 mol.% Fe. However, the relatively small volume fraction of Fp (20 vol.%) in the lower mantle suggests that the electronic contribution of Fp to the total thermal conductivity of the lowermost mantle is insignificant ( $\sim 0.2$  W/m/K). Accordingly, our estimate of the total thermal conductivity of a pyrolitic mantle ( $k_{total} = 4$ - $11$  W/m/K) only accounts for the radiative ( $k_{rad} = 1$  W/m/K, this work) and lattice contributions (3-10 W/m/K at CMB, previous studies (Geballe et al., 2020; Hsieh et al., 2018; Ohta et al., 2017; Okuda et al., 2017; Stackhouse et al., 2015; Tang et al., 2014). Using our estimate of total thermal conductivity in Eq. (1) we obtain  $Q_{CMB} = 1.5$ - $27$  TW for the temperature gradients in the TBL of 0.0025-0.016 K/m (Lay et al., 2008; van der Hilst

et al., 2007). That is, the approach based on the Fourier law of heat conduction yields a factor of twenty uncertain  $Q_{CMB}$ . While being broadly consistent with the estimates based on the core and mantle dynamics of  $Q_{CMB} = 8\text{--}16$  TW (Lay et al., 2008; Nimmo, 2015), this result highlights the need for more accurate constraints on thermal conductivity and, especially, temperature gradients in the TBL at the base of the mantle. We note, however, that the apparent invariance of  $k_{rad}$  to  $T$  found here implies that heat transport by light radiation has remained relatively inefficient throughout geological time and could not have promoted a higher  $Q_{CMB}$  in the hotter ancient Earth.

In addition to the heat transport across the CMB, our results offer a cross-check on the geodesy-based inference of high electrical conductance ( $10^8$  S) layer 10–150 km above the core. Here we showed that Bgm is insulating under near-CMB conditions as it remains relatively transparent in the visible range even at  $T \sim 4000$  K; thus, the potentially high DC conductivity of the lowermost mantle cannot be due to Bgm. This is also supported by previous studies that inferred a relatively low Bgm (and post-perovskite) electrical conductivity ( $\sim 0.01\text{--}0.03$  S/cm) at high  $P$ - $T$  conditions (Ohta et al., 2008; Sinmyo et al., 2014). In contrast to Bgm, the measured absorption coefficients of Fp imply that its DC conductivity is much higher than that of Bgm at near CMB conditions. The computed electrical conductivities of  $(Mg_{0.875}, Fe_{0.125})O$  at 135 GPa and 4300 K span  $\sim 45\text{--}165$  S/cm (Fig. S8), depending mainly on the band gap correction used in the computation. This result is not only consistent with the recent theoretical estimates (Holmstrom et al., 2018), but it falls within the range of DC conductivities required to produce the conductance of  $10^8$  S in a 50–150 km thick mechanical mixture of insulating Bgm (80 vol.%) with conducting Fp (20 vol.%) (Fig. 5B). The necessary electrical conductance may be achieved even in a thin (e.g. < 50 km) layer just above the core if the electrical conductivity of Fp is greater than 100 S/cm. The results of this work together with previous first-principles computations (Holmstrom et al., 2018) are consistent with such high electrical conductivity in iron-enriched Fp (> 20 mol.% Fe), which could be a plausible explanation for the six year oscillation in the length of day (Buffett, 1992; Holme and de Viron, 2013). Seismic tomography images have revealed patches of ULVZs that could be explained by the occurrence of iron-enriched Fp (Wicks et al., 2017). If such, these regions implement strongest core-mantle electromagnetic coupling and may manifest themselves in geomagnetic features observable at the Earth's surface. A large ULVZ located beneath the Central Pacific may electromagnetically screen the varying field of the core (Buffett, 2015; Runcorn, 1992), which would explain the anomalously low geomagnetic secular variations observed in this region at least over the past 10–100 Ka (Constable et al., 2016; Panovska et al., 2018). Likewise, electric currents in a ULVZ triggered by rapid changes in the orientation of the magnetic dipole during geomagnetic reversals may generate a torque on the core and guide the reversing dipole along the meridians that border the ULVZ (Buffett, 2015; Runcorn, 1992). Therefore, the preference of reversal paths that border the Pacific Ocean may be due to the ULVZ detected beneath the Pacific.

Overall, our results underscore the link between radiative and electrical conductivity. Moderately opaque and electrically insulating Bgm has small but non-negligible radiative thermal conductivity the magnitude of which determines the radiative heat flux in the lowermost mantle. Highly opaque Fp has negligible radiative thermal conductivity but its semi-metallic electrical conductivity is sufficient to implement efficient core-mantle electromagnetic coupling. Therefore, possible variations in the mineralogical abundances of these minerals along the CMB (e.g. in the basaltic and pyrolytic compositions) provide the means for heterogeneous CMB thermal and electromagnetic interaction. Strongest core-mantle

electromagnetic interaction is expected in regions where Fp is present at the CMB, which may be detected in the secular signal of Earth's magnetic field.

### CRediT authorship contribution statement

**Sergey S. Lobanov:** Conceptualization, Methodology, Investigation, Formal Analysis, Writing.

**François Soubiran:** Software, Investigation, Writing.

**Nicholas Holtgrewe:** Software, Investigation.

**James Badro:** Resources, Writing.

**Jung-Fu Lin:** Resources, Writing.

**Alexander F. Goncharov:** Conceptualization, Methodology, Writing.

### Declaration of competing interest

The authors declare that they have no known competing financial interests or personal relationships that could have appeared to influence the work reported in this paper.

### Acknowledgements

SSL acknowledges the support of the Helmholtz Young Investigators Group CLEAR (VH-NG-1325). The authors thank T. Okuchi and N. Purevjav in synthesis of Fp and Bgm samples. FS was supported by a Marie Skłodowska-Curie Actions under the project ABISSE (grant agreement no. 750901). The work at Carnegie was supported by the NSF (grant numbers DMR-1039807, EAR-1520648, EAR/IF-1128867, EAR-1763287, and EAR-2049127), the Army Research Office (grant 56122-CH-H), the Deep Carbon Observatory, and the Carnegie Institution of Washington. Numerical simulations were performed on the GENCI supercomputer Occigen through the stl2816 series of eDARI computing grants. JFL acknowledges support by the NSF Geophysics Program (EAR-1446946 and EAR-1916941). JB acknowledges support by IPGP multidisciplinary program PARI, by Region Île de France SESAME Grant no. 12015908, and by Université de Paris UnivEarthS Labex program (ANR-10-LABX-0023 and ANR-11-IDEX-0005-02).

### Appendix A. Supplementary material

Supplementary material related to this article can be found online at <https://doi.org/10.1016/j.epsl.2021.116871>.

### References

- Akahama, Y., Kawamura, H., 2006. Pressure calibration of diamond anvil Raman gauge to 310 GPa. *J. Appl. Phys.* 100, 043516.
- Ammann, M.W., Brodholt, J.P., Dobson, D.P., 2011. Ferrous iron diffusion in ferropericlase across the spin transition. *Earth Planet. Sci. Lett.* 302, 393–402.
- Buffett, B.A., 1992. Constraints on magnetic energy and mantle conductivity from the forced nutations of the Earth. *J. Geophys. Res., Solid Earth* 97, 19581–19597.
- Buffett, B.A., 2015. 8.08 - Core-mantle interactions. In: Schubert, G. (Ed.), *Treatise on Geophysics*, second edition. Elsevier, Oxford, pp. 213–224.
- Burns, R.G., 1993. *Mineralogical Applications of Crystal Field Theory*, 2nd ed. Cambridge University Press, U.K.
- Clark, S.P., 1957. Radiative transfer in the Earth's mantle. *Eos Trans. AGU* 38, 931–938.
- Constable, C., Korte, M., Panovska, S., 2016. Persistent high paleosecular variation activity in southern hemisphere for at least 10 000 years. *Earth Planet. Sci. Lett.* 453, 78–86.
- Garnero, E.J., McNamara, A.K., 2008. Structure and dynamics of Earth's lower mantle. *Science* 320, 626–628.
- Geballe, Z.M., Sime, N., Badro, J., van Keken, P.E., Goncharov, A.F., 2020. Thermal conductivity near the bottom of the Earth's lower mantle: measurements of pyrolyte up to 120 GPa and 2500 K. *Earth Planet. Sci. Lett.* 536, 116161.
- Goncharov, A.F., Beck, P., Struzhkin, V.V., Haugen, B.D., Jacobsen, S.D., 2009. Thermal conductivity of lower-mantle minerals. *Phys. Earth Planet. Inter.* 174, 24–32.

- Goncharov, A.F., Crowhurst, J.C., Dewhurst, J.K., Sharma, S., Sanloup, C., Gregoryanz, E., Guignot, N., Mezouar, M., 2007. Thermal equation of state of cubic boron nitride: implications for a high-temperature pressure scale. *Phys. Rev. B* 75, 224114.
- Goncharov, A.F., Haugen, B.D., Struzhkin, V.V., Beck, P., Jacobsen, S.D., 2008. Radiative conductivity in the Earth's lower mantle. *Nature* 456, 231–234.
- Goncharov, A.F., Lobanov, S.S., Tan, X., Hohensee, G.T., Cahill, D.G., Lin, J.F., Thomas, S.M., Okuchi, T., Tomioka, N., 2015. Experimental study of thermal conductivity at high pressures: implications for the deep Earth's interior. *Phys. Earth Planet. Inter.* 247, 11–16.
- Haigis, V., Salanne, M., Jahn, S., 2012. Thermal conductivity of MgO, MgSiO<sub>3</sub> perovskite and post-perovskite in the Earth's deep mantle. *Earth Planet. Sci. Lett.* 355, 102–108.
- Hashin, Z., Shtrikman, S., 1962. A variational approach to theory of effective magnetic permeability of multiphase materials. *J. Appl. Phys.* 33, 3125–3131.
- Hofmeister, A.M., 2014. Thermodynamic and optical thickness corrections to diffusive radiative transfer formulations with application to planetary interiors. *Geophys. Res. Lett.* 41, 3074–3080.
- Holme, R., de Viron, O., 2013. Characterization and implications of intradecadal variations in length of day. *Nature* 499, 202–205.
- Holmstrom, E., Stixrude, L., Scipioni, R., Foster, A.S., 2018. Electronic conductivity of solid and liquid (Mg, Fe)O computed from first principles. *Earth Planet. Sci. Lett.* 490, 11–19.
- Hsieh, W.P., Deschamps, F., Okuchi, T., Lin, J.F., 2017. Reduced lattice thermal conductivity of Fe-bearing bridgmanite in Earth's deep mantle. *J. Geophys. Res., Solid Earth* 122, 4900–4917.
- Hsieh, W.P., Deschamps, F., Okuchi, T., Lin, J.F., 2018. Effects of iron on the lattice thermal conductivity of Earth's deep mantle and implications for mantle dynamics. *Proc. Natl. Acad. Sci. USA* 115, 4099–4104.
- Hummer, D.R., Fei, Y.W., 2012. Synthesis and crystal chemistry of Fe<sup>3+</sup>-bearing (Mg, Fe<sup>3+</sup>)(Si, Fe<sup>3+</sup>)O<sub>3</sub> perovskite. *Am. Mineral.* 97, 1915–1921.
- Jiang, S.Q., Holtgrewe, N., Lobanov, S.S., Su, F.H., Mahmood, M.F., McWilliams, R.S., Goncharov, A.F., 2018. Metallization and molecular dissociation of dense fluid nitrogen. *Nat. Commun.* 9, 2624.
- Keppler, H., Dubrovinsky, L.S., Narygina, O., Kantor, I., 2008. Optical absorption and radiative thermal conductivity of silicate perovskite to 125 Gigapascals. *Science* 322, 1529–1532.
- Lay, T., Hernlund, J., Buffett, B.A., 2008. Core-mantle boundary heat flow. *Nat. Geosci.* 1, 25–32.
- Lobanov, S.S., Goncharov, A.F., Litasov, K.D., 2015. Optical properties of siderite (FeCO<sub>3</sub>) across the spin transition: crossover to iron-rich carbonates in the lower mantle. *Am. Mineral.* 100, 1059–1064.
- Lobanov, S.S., Holtgrewe, N., Goncharov, A.F., 2016. Reduced radiative conductivity of low spin FeO<sub>6</sub>-octahedra in FeCO<sub>3</sub> at high pressure and temperature. *Earth Planet. Sci. Lett.* 449, 20–25.
- Lobanov, S.S., Holtgrewe, N., Ito, G., Badro, J., Piet, H., Nabiei, F., Lin, J.-F., Bayarjargal, L., Wirth, R., Schreiber, A., Goncharov, A.F., 2020. Blocked radiative heat transport in the hot pyrolytic lower mantle. *Earth Planet. Sci. Lett.* 537, 116176.
- Lobanov, S.S., Holtgrewe, N., Lin, J.F., Goncharov, A.F., 2017a. Radiative conductivity and abundance of post-perovskite in the lowermost mantle. *Earth Planet. Sci. Lett.* 479, 43–49.
- Lobanov, S.S., Hsu, H., Lin, J.F., Yoshino, T., Goncharov, A.F., 2017b. Optical signatures of low spin Fe<sup>3+</sup> in NAL at high pressure. *J. Geophys. Res., Solid Earth* 122, 3565–3573.
- Lobanov, S.S., Speziale, S., 2019. Radiometric temperature measurements in nongray ferropericlasite with pressure- spin- and temperature-dependent optical properties. *J. Geophys. Res., Solid Earth* 124, 12825–12836.
- Manthilake, G.M., de Koker, N., Frost, D.J., McCammon, C.A., 2011. Lattice thermal conductivity of lower mantle minerals and heat flux from Earth's core. *Proc. Natl. Acad. Sci. USA* 108, 17901–17904.
- Mao, Z., Wang, F., Lin, J.F., Fu, S.Y., Yang, J., Wu, X., Okuchi, T., Tomioka, N., Prakapenka, V.B., Xiao, Y.M., Chow, P., 2017. Equation of state and hyperfine parameters of high-spin bridgmanite in the Earth's lower mantle by synchrotron X-ray diffraction and Mossbauer spectroscopy. *Am. Mineral.* 102, 357–368.
- McWilliams, R.S., Dalton, D.A., Mahmood, M.F., Goncharov, A.F., 2016. Optical properties of fluid hydrogen at the transition to a conducting state. *Phys. Rev. Lett.* 116, 255501.
- Montoya, J.A., Goncharov, A.F., 2012. Finite element calculations of the time dependent thermal fluxes in the laser-heated diamond anvil cell. *J. Appl. Phys.* 111, 112617.
- Nimmo, F., 2015. 8.02 - Energetics of the core. In: Schubert, G. (Ed.), *Treatise on Geophysics*, second edition. Elsevier, Oxford, pp. 27–55.
- Ohta, K., Onoda, S., Hirose, K., Sinmyo, R., Shimizu, K., Sata, N., Ohishi, Y., Yasuhara, A., 2008. The electrical conductivity of post-perovskite in Earth's D" layer. *Science* 320, 89–91.
- Ohta, K., Yagi, T., Hirose, K., Ohishi, Y., 2017. Thermal conductivity of ferropericlasite in the Earth's lower mantle. *Earth Planet. Sci. Lett.* 465, 29–37.
- Ohta, K., Yagi, T., Taketoshi, N., Hirose, K., Kornabayashi, T., Baba, T., Ohishi, Y., Hernlund, J., 2012. Lattice thermal conductivity of MgSiO<sub>3</sub> perovskite and post-perovskite at the core-mantle boundary. *Earth Planet. Sci. Lett.* 349, 109–115.
- Okuda, Y., Ohta, K., Hasegawa, A., Yagi, T., Hirose, K., Kawaguchi, S.I., Ohishi, Y., 2020. Thermal conductivity of Fe-bearing post-perovskite in the Earth's lowermost mantle. *Earth Planet. Sci. Lett.* 547, 116466.
- Okuda, Y., Ohta, K., Yagi, T., Sinmyo, R., Wakamatsu, T., Hirose, K., Ohishi, Y., 2017. The effect of iron and aluminum incorporation on lattice thermal conductivity of bridgmanite at the Earth's lower mantle. *Earth Planet. Sci. Lett.* 474, 25–31.
- Panovska, S., Constable, C.G., Korte, M., 2018. Extending global continuous geomagnetic field reconstructions on timescales beyond human civilization. *Geochem. Geophys. Geosyst.* 19, 4757–4772.
- Runcorn, S.K., 1992. Polar path in geomagnetic reversals. *Nature* 356, 654–656.
- Shankland, T.J., Nitsan, U., Duba, A.G., 1979. Optical absorption and radiative heat transport in olivine at high temperature. *J. Geophys. Res.* 84, 1603–1610.
- Sinmyo, R., Pesce, G., Greenberg, E., McCammon, C., Dubrovinsky, L., 2014. Lower mantle electrical conductivity based on measurements of Al, Fe-bearing perovskite under lower mantle conditions. *Earth Planet. Sci. Lett.* 393, 165–172.
- Stackhouse, S., Stixrude, L., Karki, B.B., 2015. First-principles calculations of the lattice thermal conductivity of the lower mantle. *Earth Planet. Sci. Lett.* 427, 11–17.
- Syassen, K., 2008. Ruby under pressure. *High Press. Res.* 28, 75–126.
- Tang, X.L., Ntam, M.C., Dong, J.J., Rainey, E.S.G., Kavner, A., 2014. The thermal conductivity of Earth's lower mantle. *Geophys. Res. Lett.* 41, 2746–2752.
- van der Hilst, R.D., de Hoop, M.V., Wang, P., Shim, S.H., Ma, P., Tenorio, L., 2007. Seismostratigraphy and thermal structure of Earth's core-mantle boundary region. *Science* 315, 1813–1817.
- Wicks, J.K., Jackson, J.M., Sturhahn, W., Zhang, D.Z., 2017. Sound velocity and density of magnesio-wustites: implications for ultralow-velocity zone topography. *Geophys. Res. Lett.* 44, 2148–2158.